Nanoscale

PAPER

View Article Online
View Journal | View Issue

Cite this: *Nanoscale*, 2023, **15**, 2417

Crystal phase engineering of Ru for simultaneous selective photocatalytic oxidations and H_2 production†

Michaël Gebruers,‡[a] Chunhua Wang, ‡[b] Rafikul A. Saha,[a] Yangshan Xie,[a] Imran Aslam, [a] Li Sun, [b] Yuhe Liao,[c] Xuhui Yang, [d] Taoran Chen,[d] Min-Quan Yang, [d] Bo Weng *[a] and Maarten B. J. Roeffaers *[a]

Noble metal nanoparticles are often used as cocatalysts to enhance the photocatalytic efficiency. While the effect of cocatalyst nanoparticle size and shape has widely been explored, the effect of the crystal phase is largely overlooked. In this work, we investigate the effect of Ru nanoparticle crystal phase, specifically regular hexagonal close-packed (hcp) and allotropic face-centered cubic (fcc) crystal phases, as cocatalyst decorated onto the surface of TiO_2 photocatalysts. As reference photocatalytic reaction the simultaneous photocatalytic production of benzaldehyde (BAD) and H_2 from benzyl alcohol was chosen. Both the fcc Ru/TiO_2 and hcp Ru/TiO_2 composites exhibit enhanced BAD and H_2 production rates compared to pristine TiO_2 due to the formation of a Schottky barrier promoting the photogenerated charge separation. Moreover, a 1.9-fold photoactivity enhancement of the fcc Ru/TiO_2 composite is achieved as compared to the hcp Ru/TiO_2 composite, which is attributed to the fact that the fcc Ru NPs are more efficient in facilitating the charge transfer as compared to hcp Ru NPs, thus inhibiting the recombination of electron–hole pairs and enhancing the overall photoactivity.

Received 17th November 2022,
Accepted 12th January 2023

DOI: 10.1039/d2nr06447b

rsc.li/nanoscale

1 Introduction

Inorganic semiconductors, such as TiO_2, are often preferred as photocatalysts (PCs) due to their relatively low price, high stability, and non-toxicity.[1–3] One of the major drawbacks is the rapid photogenerated charge carrier recombination, leaving room for further improvement to maximize the photocatalytic activity.[4] The addition of noble metal nanoparticles (NPs) as cocatalyst can not only slow down the electron–hole recombination by trapping photogenerated charges,[5–8] they can also provide catalytically active sites.[9–11] Therefore metal NP cocatalysts are crucial in the development of improved semiconductor PCs.

Various noble metal NPs have been reported as cocatalysts to increase the photocatalytic activity of TiO_2, including Pt,[12] Au,[13] and Ru.[14] Of these noble metals, Ru is of specific interest due to its relatively low price compared to the other noble metals,[15] and its proven efficiency as a cocatalyst in metal-based composite catalysed photocatalysis.[16,17] Usually, the properties of Ru NPs are fine-tuned *via* size and shape engineering.[18] However, the properties of Ru NPs can also be tuned by engineering its crystal phase. In bulk Ru adopts a hexagonal close-packed (hcp) phase, recently Ru NPs with a face-centered cubic (fcc) phase have been reported.[19] Crystal phase engineering offers an efficient approach to modulate the physicochemical properties of (noble) metal NPs.[20–24] For instance, Ye *et al.* studied the performance of hcp and fcc Ru cocatalysts supported on C_3N_4 for the photocatalytic CO_2 to fuel conversion.[25] It was demonstrated that hcp Ru results in increased selectivity for the formation of CO and CH_4, while fcc Ru causes an increased selectivity for the formation of H_2. Recently, dual-functional photocatalytic reaction systems to simultaneously trigger the reduction and oxidation reaction for achieving both reduction and oxidation productions have received extensive attention.[26] However, the utilization of Ru NPs for dual-functional photocatalysis in the simultaneous production of solar fuels and organic molecules has never been reported. It is therefore of importance to study the

[a]*cMACS, Department of Microbial and Molecular Systems, KU Leuven, Celestijnenlaan 200F, 3001 Leuven, Belgium. E-mail: bo.weng@kuleuven.be, maarten.roeffaers@kuleuven.be*
[b]*Department of Chemistry, KU Leuven, Celestijnenlaan 200F, 3001 Leuven, Belgium*
[c]*Guangzhou Institute of Energy Conversion, Chinese Academy of Sciences, No. 2, Nengyuan, Road, Tianhe District, Guangzhou 510641, P.R. China*
[d]*College of Environmental Science and Engineering, Fujian Key Laboratory of Pollution Control & Resource Reuse, Fujian Normal University, Fuzhou 350007, P.R. China*

†Electronic supplementary information (ESI) available. See DOI: https://doi.org/10.1039/d2nr06447b

‡These authors contributed equally to this work.

photocatalytic properties of Ru NPs as cocatalysts to establish a structure–function relationship in dual-functional photocatalytic reaction systems toward the production of value-added chemicals.

2 Experimental section

2.1 Chemicals and reagents

Triethylene glycol (99.0%), ruthenium(III) acetylacetonate (99.9%) and trifluorotoluene (90.0%) were obtained from Alfa Aesar, ruthenium(III) chloride (99.9%) acetone (99.8%), benzyl alcohol (99.0%), Hexane (≥97.0%) and diethyl ether (≥99.5%) from Acros organics, ethylene glycol (≥98.0%) from Carl Roth, polyvinylpyrrolidone (30 k) from MP biomedicals, ethanol (99.8%) from Fisher, titanium oxide (21 nm, ≥99.5%) and Ammonium oxalate (≥99.0%) from Sigma-Aldrich, sodium sulfate (≥99.0%) from Merck, potassium persulfate (99.0%) from Chimica. All chemicals were used as obtained from the supplier.

2.2 Synthesis of allotropic Ru NPs

Ru NPs with a fcc and hcp crystal phase were synthesized by a method based on the work by Kusada *et al.*[19] Ru NPs with different crystal phases were synthesized by changing the Ru precursor and the type of solvent and reductant in the synthesis. The Ru NPs were synthesized *via* a chemical reduction method by using $Ru(AcAc)_3$ as the Ru precursor for the synthesis of fcc Ru and $RuCl_3{\cdot}H_2O$ as the Ru precursor for hcp Ru. Triethyleneglycol (TEG) and ethylene glycol (EG) were used as the solvent and reducing agent for the synthesis of fcc and hcp Ru NPs respectively. Polyvinylpyrrolidone (PVP) was added as a stabilizing agent to avoid agglomeration of the NPs. In a typical synthesis the Ru precursor and PVP are suspended in TEG or EG at room temperature. This solution is then refluxed at 180 °C for 3 hours under continuous steering (600 rpm) in an oil bath. After 3 hours the reaction mixture was cooled down to room temperature by removing it from the oil bath. The Ru NPs were then separated from the reaction mixture by adding diethyl ether and acetone and centrifugation at 7000 rpm for 2 minutes. The Ru NPs were then washed with ethanol and diethyl ether and dried overnight under vacuum at 55 °C.

2.3 Catalyst loading

Ru/TiO_2 composites were prepared *via* a wet impregnation method. The following method was used to prepare 0.60 wt% Ru/TiO_2 composites; 1.2 mL of a Ru NPs suspension in ethanol (1 mg mL^{-1}) was added to a suspension of 200 mg of TiO_2 in 20 mL hexane : ethanol (3 : 1). The mixture was stirred for 16 h (400 rpm) at room temperature. The catalysts were separated from the reaction mixture *via* centrifugation at 3500 rpm for 5 minutes and washed three times with hexane. Finally, the Ru/TiO_2 composites were dried overnight at 55 °C. Ru/TiO_2 composites with different amounts of Ru loading were prepared by adjusting the amount of TiO_2 and the volume of Ru NPs suspension added to the synthesis mixture.

2.4 Characterization

2.4.1 X-ray diffraction (XRD). The synthesized Ru NPs were characterized by powder X-ray diffraction (PXRD) to determine their crystal phase. Powder X-ray diffractograms were recorded on a Malvern PANalytical Empyrean diffractometer equipped with a PIXcel3D solid state detector using a Cu anode (Cu Kα1: 1.5406 Å; Cu Kα2: 1.5444 Å). Samples were loaded onto a 96-well sample holder and X-ray diffractograms were recorded at room temperature in transmission geometry (Debye-Scherrer; θ–θ scan) within a 1.3°–70° 2θ range using a step size of 0.013°.

2.4.2 Transmission electron microscopy (TEM). Transmission electron microscopy (TEM) measurements were performed to determine the size of the Ru NPs. TEM images were obtained by a FEI Talos F200s instrument at an acceleration voltage of 200 kV.

2.4.3 Wavelength dispersive X-ray fluorescence (WDXRF). The Ru loaded catalysts were analysed with wavelength dispersive X-ray fluorescence (WDXRF) to determine the amount of Ru loading of the catalyst materials. Samples were transferred to a Teflon cup with a 4 mm opening sealed with a Prolene thin-film and analysed on a Bruker S8 TIGER 4k.

2.4.4 Raman spectroscopy. Raman measurements were performed at room temperature on a confocal Raman microscope (MonoVista CRS+, S&I instruments). The 532 nm laser line (Cobolt Samba) was used as the excitation source, the laser beam was focused on the sample with a 100× 0.9NA objective lens (MPLN100X, Olympus). After collecting the signal with the same objective lens, the backward Raman scattering signal passed through a 100 μm confocal pinhole into the monochromator (Princeton Instruments) equipped with a 1200 grooves per nm grating. The signal was recorded with a CCD camera (Newton 920, Andor). The spectra of the catalyst materials were obtained by averaging 5 acquisitions.

2.4.5 UV-VIS diffuse reflectance spectroscopy (DRS). UV-VIS diffuse reflectance spectra of the catalyst materials were recorded on a PerkinElmer Lambda 950 UV-VIS-NIR spectrophotometer with a 150 mm integrated sphere in the wavelength range between 300 and 700 nm.

2.4.6 Photoelectrochemical characterization. Photoelectrochemical analysis was carried out in a three-electrode quartz cell with an Ag/AgCl electrode as a reference electrode and a Pt plate as a counter electrode. The working electrodes were prepared on fluorine-doped tin oxide (FTO) glass cleaned by ultrasonication in ethanol and in water for 30 min and dried under a N_2 flow. A catalyst suspension was prepared by dispersing 10 mg of catalyst in 1 mL of ethanol under ultrasonication. Then, 20 μL of the catalyst suspension was dropped onto the FTO substrate where the exposed area of the working electrode was fixed at 0.25 cm^2 by using Scotch tape to protect the boundary of the FTO substrate. After drying in air, the working electrodes were dried at 80 °C for 2 h to enhance adhesion.

Linear sweep voltammetry (LSV) was carried out on an electrochemical workstation (Bio-Logic SP-200). The cathodic

polarization curves were obtained by using the linear sweep voltammetry technique with a scan rate of 0.5 mVs^{-1} in an aqueous 0.2 M Na_2SO_4 solution. The electrochemical impedance spectroscopy (EIS) experiments were conducted on an electrochemical workstation (CHI660E) in an aqueous 0.2 M Na_2SO_4 solution (pH = 6.8) under a frequency range from 0.01 Hz to 100 kHz under open circuit potential.

2.4.7 Photoluminescence (PL) spectroscopy. Photoluminescence (PL) spectra of the catalyst materials were recorded on an Edinburgh FLS980 photoluminescence spectrometer from 400 to 550 nm with an integration time of 1 nm s^{-1} under an excitation wavelength of 255 nm.

2.4.8 Electron paramagnetic resonance (EPR). Electron paramagnetic pair (EPR) spectra were recorded on a Magnettech ESR5000X spectrometer. First, 5 mg of catalyst material was dispersed in a solution of 1 mL CH_3CN containing 20 μL benzyl alcohol and 0.5 mmol of 5,5-dimethyl-1-pyrroline-*N*-oxide (DMPO). This suspension was then transferred to a glass capillary and placed in a sealed glass tube under argon atmosphere. The sealed glass tube is then placed in the microwave cavity of the EPR spectrometer and irradiated by a 300 W Xenon lamp at room temperature.

2.5 Photocatalytic activity measurements

In a typical experiment 104 μL of benzyl alcohol, 2.5 mL of trifluorotoluene and 15 mg of catalyst were added in a glass reactor. For the control experiments, 50 μL of a scavenger in trifluorotoluene solution (1 mM) was added to the reaction mixture. The reactor was sealed and put under vacuum. The mixture was then irradiated under continuous steering (500 rpm) for 14 h under irradiation of a 300 W Xe lamp with an AM 1.5 G filter to simulate the solar light spectrum. After irradiation, 1 mL of the headspace gas was analysed by an Agilent 7890B instrument equipped with a methane convertor, a MolSieve 5A and a Porapak Q column and a thermal conductivity detector (TCD) and flame ionization detector (FID). The reaction mixture was prepared for liquid phase analysis by separating the reaction mixture from the catalyst *via* centrifugation for 5 minutes (8000 rpm) and transferring 1 mL of the solution to a GC vial. This solution was analysed with gas chromatography (GC), on a Shimadzu 2010 GC CP-Sil 5 with an FID detector.

2.6 Density-functional theory (DFT) calculations

The first-principle calculation were conducted through the Vienna *ab initio* Simulation Package (VASP) using projector-augmented wave (PAW) method.[27] The generalized gradient approximation (GGA)[28] externalized by the Perdew–Burke–Ernzerhof (PBE) approximation was used for the influence of the exchange-correction potentials.[29] A plane-wave cutoff energy was set as 600 eV, and the Γ-centered *K*-points mesh of $2\pi \times 0.02$ $Å^{-1}$ was set. The convergence criteria for energy and maximum force were set to 10^{-6} eV and 0.01 eV $Å^{-1}$, respectively. The (111) surface of the fcc-phase and (101) surface of the hcp-phase Ru were built by two 6-layer slab models with a vacuum of 25 Å. For absorption systems, to simulate the adsorption on the Ru surface, the three top atomic layers were relaxed and the other bottom layers were fixed.

3 Results and discussion

3.1 Synthesis of hcp and fcc Ru NPs

Ru NPs with a fcc and hcp structure were synthesized *via* the polyol method developed by Kusada *et al.*[19] The NP crystal phase was confirmed *via* XRD (Fig. 1A). Le-bail fitting of the XRD data was performed to determine the exact peak positions and corresponding *hkl* planes for both crystal phases. The F(111), F(200) and F(220) reflections were found at 41°, 47° and 69°, respectively, matching the peak positions reported for fcc Ru NPs;[30] for hcp Ru, the H(100), H(002) and H(101) reflections were found at 38°, 42° and 44°, respectively.[31] The latter two peaks are merged into one broad peak centered at 43°; this is in agreement with earlier reports of small (<5 nm) hcp Ru NPs.[32–34] The size of the as-synthesized Ru NPs was determined *via* TEM measurements, as shown in Fig. S1 and S2 (ESI†). Both fcc and hcp Ru NPs appear spherical in shape and have a size of 2.7 ± 0.4 nm and 2.6 ± 0.4 nm, respectively.

3.2 Structural characterization of hcp and fcc Ru/TiO_2 composites

The fcc and hcp Ru NPs were decorated onto the surface of TiO_2 *via* a wet impregnation method. The exact amount of Ru NPs in the Ru/TiO_2 composites was confirmed by wavelength dispersive X-ray fluorescence (WDXRF), as summarised in Table S1 (ESI†).

The XRD patterns of the different Ru/TiO_2 composites are shown in Fig. S3 (ESI†), and all identified peaks can be assigned to TiO_2. No diffraction peaks related to the presence

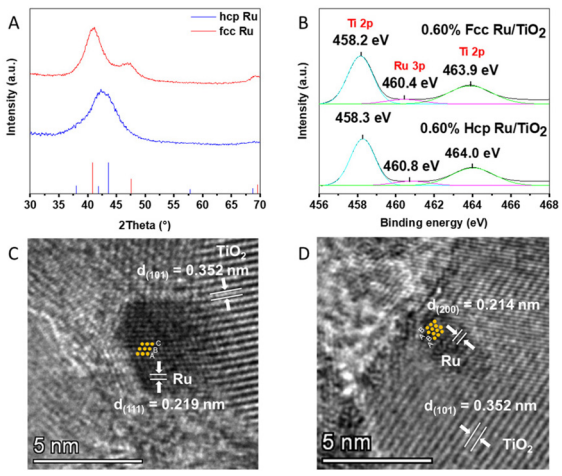

Fig. 1 (A) X-ray diffractograms of the as synthesized fcc and hcp Ru NPs. Red and blue lines represent the locations of characteristic peaks of fcc Ru (JCPDS no. 88-2333) and hcp Ru (JCPDS no. 06-0663), respectively. (B) High-resolution XPS spectra of the core levels of Ru 3p in 0.60 wt% hcp Ru/TiO_2 and 0.60 wt% fcc Ru/TiO_2. HRTEM images of (C) 0.60 wt% fcc Ru/TiO_2 and (D) 0.60 wt% hcp Ru/TiO_2.

of Ru NPs are visible, which is due to the low Ru loading (*ca.* 0.60 wt%). The phase composition of the Ru/TiO_2 PCs was further analysed by Raman spectroscopy. As shown in Fig. S4 (ESI†), the Raman spectrum of TiO_2 shows five resonances which correspond to the anatase vibration modes of TiO_2: 146 cm^{-1} (E_g), 198 cm^{-1} (E_g), 399 cm^{-1} (B_g), 519 cm^{-1} (A_g/B_g) and 639 cm^{-1} (E_g). Notably, the peak located at 146 cm^{-1}, representing the symmetric O–Ti–O stretching,[35] is shifted towards higher wavenumbers upon functionalization with Ru NPs. This blue-shift is attributed to a microscopic structural disorder of the oxygen lattice caused by Ru loading,[36] caused by a strong interaction between the Ru NPs and TiO_2.

TEM images of the Ru/TiO_2 composites in Fig. S5 (ESI†) show that both the fcc and hcp Ru NPs are evenly distributed on the TiO_2 particles in the respective samples, and that they maintained their size upon impregnation (Fig. S6 (ESI†)) with no visible signs of coagulation. Furthermore, the crystal phases of both fcc and hcp Ru were determined by HRTEM analysis of the Ru/TiO_2 composites, as shown in Fig. 1C and D. A clear ABAB stacking sequence is observed for hcp Ru in the hcp Ru/TiO_2 composite while the HRTEM image of fcc Ru/TiO_2 composite reveals the fcc stacking sequence of Ru, *i.e.*, ABC. The lattice spacing of 0.352 nm, determined *via* Fourier transform of the TEM images, in these samples corresponds to the (101) plane of anatase TiO_2.[37] The valence states of the elements in the Ru/TiO_2 composites were confirmed by XPS, as shown in Fig. 1B and Fig. S7 (ESI†). The peak located at 460.4 eV corresponds to Ru $3p_{3/2}$, confirming the metallic nature of Ru in the Ru/TiO_2 composites.[38] The other two peaks located at approximately 458.2 and 463.9 eV originate from Ti $2p_{3/2}$ and Ti $2p_{1/2}$, respectively.[39]

The optical absorption of 0.60 wt% hcp Ru/TiO_2, 0.60 wt% fcc Ru/TiO_2 and TiO_2 was characterized *via* diffuse reflectance spectroscopy. As shown in Fig. S8 (ESI†), both the Ru/TiO_2 composites exhibit a similar UV absorption fingerprint as the pure TiO_2 PC. Notably, both the 0.60 wt% hcp Ru/TiO_2 and 0.60 wt% fcc Ru/TiO_2 composites show increased absorption in the visible light region compared to TiO_2, which is derived from the light scattering and interband transitions in Ru NPs.[15,40]

3.3 Photocatalytic activity of the hcp and fcc Ru/TiO_2 composites

The performance of the PCs *i.e.* pure TiO_2 and the Ru/TiO_2 composites were compared by performing the simultaneous benzaldehyde (BAD) and H_2 production from benzyl alcohol in trifluorotoluene under simulated solar illumination (AM 1.5), shown in Scheme 1.

As shown in Fig. 2A, S9 (ESI) and Table S2 (ESI†), pristine TiO_2 has a BAD and H_2 production rate of 246 and 228 μmol g^{-1} h^{-1}, respectively; the different reaction products were confirmed by gas chromatography-mass spectrometry (Fig. S10 (ESI†)). The addition of hcp Ru NPs as cocatalysts results in a substantially increased catalytic activity. The photocatalytic activity, with 0.60 wt% hcp Ru/TiO_2 as a catalyst, resulted in a BAD and H_2 production rate of 1007 and 987 μmol g^{-1} h^{-1},

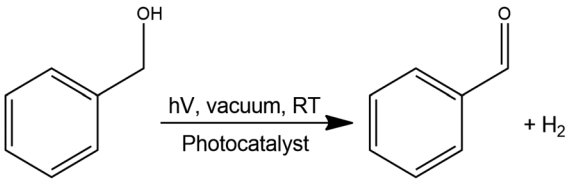

Scheme 1 General reaction for the simultaneous photocatalytic benzaldehyde (BAD) and H_2 production under simulated solar light illumination.

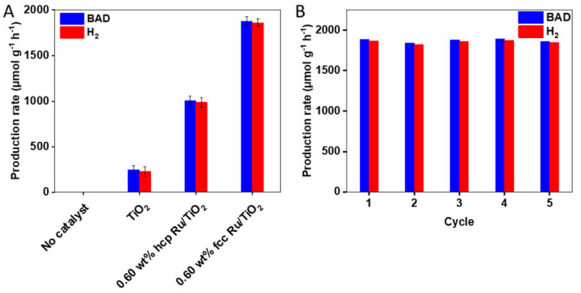

Fig. 2 (A) Catalytic performance of TiO_2, 0.60 wt% hcp Ru/TiO_2 and 0.60 wt% fcc Ru/TiO_2 in the simultaneous photocatalytic benzaldehyde (BAD) and hydrogen production from benzyl alcohol. (B) Recyclability of 0.60 wt% fcc Ru/TiO_2 in the simultaneous photocatalytic benzaldehyde (BAD) and hydrogen production from benzyl alcohol. Reaction conditions: 1.0 mmol of benzyl alcohol, 15 mg of catalyst, 2.5 mL of trifluorotoluene, under vacuum, simulated solar light (300 W Xe lamp, AM 1.5 G), reaction time of 14 h.

respectively, which is a *ca.* 4-fold increase compared to pristine TiO_2. The BAD and H_2 production rates over the 0.60 wt% fcc Ru/TiO_2 composite are approx. 1.9 times higher: 1877 and 1860 μmol g^{-1} h^{-1}, respectively. The effect of the amount of Ru loading on the catalytic activity of the fcc Ru/TiO_2 composite was investigated as well. The activity of the fcc Ru/TiO_2 composites increases with an increasing amount of Ru loading (Fig. S9 (ESI†)), until an optimum is reached at 0.60 wt% of Ru loading. The photocatalytic activity decreases again upon further increasing the Ru loading due to competitive light absorption by the metal NPs.[41]

The stability of the fcc Ru/TiO_2 catalyst was evaluated by reusing the catalyst in several consecutive experiments; Fig. 2B and Table S3 (ESI†) show the catalytic performance of 0.60 wt% fcc Ru/TiO_2 in 5 consecutives cycles (total 70 h). Both the BAD and H_2 production rate remained unchanged upon recycling and reuse, therefore it can be concluded that the catalyst is stable under the applied reaction conditions. XRD, performed on the fresh and used 0.60 wt% fcc Ru/TiO_2 composites in Fig. S11 (ESI†), does not reveal any apparent structural changes, further supporting the high stability of the 0.60 wt% fcc Ru/TiO_2 catalyst.

3.4 Origin of the improved activity of Ru/TiO_2 over pristine TiO_2

The origin of the activity enhancement by Ru loading was studied *via* photoelectrochemical characterisation.

Electrochemical impedance spectroscopy (EIS) of TiO_2 and the Ru/TiO_2 composites was carried out to determine the charge-transfer properties between the catalyst and the solution by measuring their impedance while applying an alternating current with a frequency ranging from 0.01 Hz to 100 kHz under open circuit potential. As depicted in Fig.S12 (ESI†), the radius of the arc decreases upon loading TiO_2 with Ru, with fcc Ru causing the largest reduction. A smaller arc radius means that the catalysts resistance is lower and thus possesses better charge transfer properties.[42,43] This shows that the Ru/TiO_2 composites, and especially fcc Ru/TiO_2, have a strongly reduced charge transfer resistance with the solution compared to pristine TiO_2, which leads to an enhanced photoactivity. LSV measurements were performed to measure the polarization curves and to determine the current density of the PCs. A lower overpotential at the same current density indicates a lower potential energy loss over the catalyst, resulting in a higher photocatalytic activity.[44] The polarization curves (Fig. 3A) of TiO_2 and the Ru/TiO_2 composites show the current densities of the different PCs when applying a bias potential between the working electrode (FTO coated with a thin layer of PC) and the reference electrode (Ag/AgCl). These results show that the introduction of Ru NPs strongly increases the current densities of the Ru/TiO_2 composites, compared to the bare TiO_2, at a similar potential range and decreases the overpotential, this accelerates the H_2 production kinetics, facilitating the reduction of protons into H_2, consequently, resulting in a high H_2 evolution activity.[45,46]

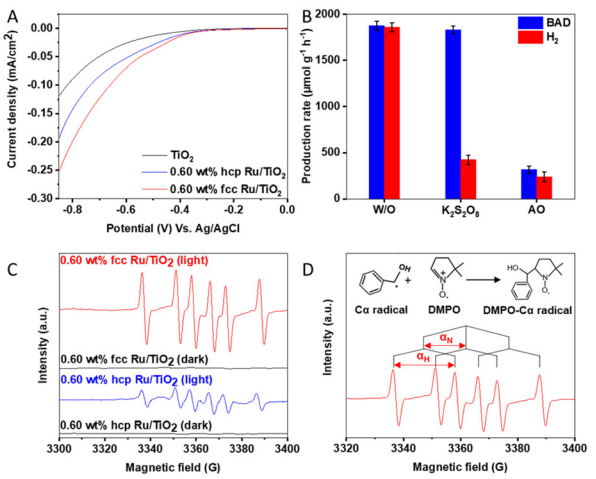

Fig. 3 (A) Polarization curves of TiO_2, 0.60 wt% hcp Ru/TiO_2 and 0.60 wt% fcc Ru/TiO_2 composites. (B) Catalytic performance of 0.60 wt% fcc Ru/TiO_2 in the absence of scavengers (W/O), in the presence of potassium persulfate ($K_2S_2O_8$) as an electron scavenger and in the presence of an ammonium oxalate (AO) as a hole scavenger in the simultaneous photocatalytic BAD and H_2 production from benzyl alcohol. (C) *In situ* EPR of 0.60 wt% fcc Ru/TiO_2 and 0.60 wt% hcp Ru/TiO_2 composites in argon saturated CH_3CN solution in the presence of DMPO with and without light irradiation. (D) Qualitative analysis of the EPR spectrum of 0.60 wt% fcc Ru/TiO_2 composites under light irradiation in which α_H = 21.8 and α_N = 15.1.

Photoluminescence measurements of TiO_2 and the Ru/TiO_2 composites were performed to probe the radiative recombination of photogenerated charge carriers.[47,48] Similar PL was observed for TiO_2 and the Ru/TiO_2 composites, as shown in Fig. S13 (ESI†). Illumination of TiO_2 with ultraviolet light results in a weak, broad visible light photoluminescence arising from the radiative recombination of charge carriers, with the emission intensity proportional to the recombination probability.[36] The diminished PL intensity of Ru/TiO_2 composites as compared with TiO_2 confirms that the decoration of Ru NPs enhances electron hole separation and reduces the radiative charge carrier recombination.[9] This is ascribed to the formation of the Schottky barrier at the Ru/TiO_2 interface,[39] with Ru acting as an electron sink, as depicted in Fig. 4. Moreover, the PL intensity of the 0.60 wt% fcc Ru/TiO_2 composite is lower than that of the 0.60 wt% hcp Ru/TiO_2 composite, which suggests a more efficient transfer of the photogenerated electrons to the Ru NPs. The increased charge carrier separation of the fcc Ru/TiO_2 composite compared to the hcp Ru/TiO_2 composite is directly caused by an increase of the Schottky barrier height, retarding the backflow of photogenerated electrons and decreasing the charge recombination rate.[49] Fig. 4 shows that the Schottky barrier height of the metal-based composite is directly related to the work function of the metal cocatalyst. Furthermore, it is reported in literature that each lattice plane has its own work function and that the work function of metal NPs is dependent on the lattice planes on the surface.[50,51] Therefore, the work function of a material is strongly dependent on its size, shape and crystal phase. The fcc and hcp Ru NPs studied in this work have a similar size and are both spherical. The difference in work function between both materials thus results from the strong difference in lattice plane composition at the surface caused by their difference in crystal phase. The work function of hcp and fcc

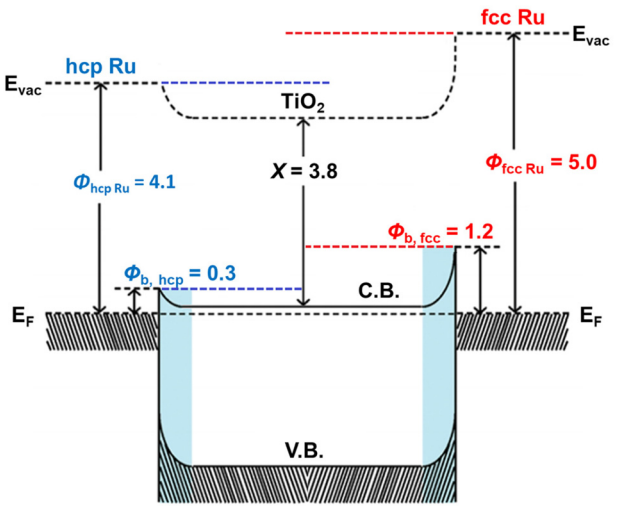

Fig. 4 Schematic energy-band diagram of hcp Ru/TiO_2 and fcc Ru/TiO_2 composites in which ϕ_{Ru} is the work function of Ru, ϕ_b the Schottky barrier height and X the electron affinity of TiO_2.

Ru was determined *via* density-functional theory (DFT) calculations of the main lattice plane of both crystal phases. The main lattice planes of hcp and fcc Ru were determined *via* analysis of the XRD data to be the H(101) and F(111) planes for hcp and fcc Ru, respectively. The optimized structures of the H(101) and F(111) lattice planes, calculated *via* DFT, are shown in Figs. S14 and S15 (ESI†). It was determined from these lattice planes that hcp and fcc Ru have a work function of 4.1 eV and 5.0 eV respectively. This results in a Schottky barrier height, determined *via* the Schottky–Mott rule,[49] of respectively 0.3 and 1.2 eV for the hcp and fcc Ru/TiO_2 composites. The enhanced photocatalytic performance of fcc Ru/TiO_2, compared to hcp Ru/TiO_2, can be directly explained by the difference in work function between the fcc and hcp Ru NPs, resulting in the different charge separation efficiency. The difference in catalytic activity of hcp and fcc Ru was further studied by calculating the H^+ and H_2 adsorption on both hcp and fcc Ru (Table S4 (ESI) and Fig. S14 (ESI†)). For this the most prominent crystal facet, as determined from XRD, for both was used *i.e.* H(101) and F(111). The increased H^+ adsorption strength on fcc Ru, compared to hcp Ru, indicates that H^+ will more strongly adsorb on fcc Ru, resulting in a higher availability of activated protons and hence probability of H_2 formation. The weaker H_2 adsorption on fcc Ru, compared to hcp Ru, suggests that fcc Ru more easily desorbs the reaction product H_2. Both support the experimentally determined increased activity of fcc Ru over hcp Ru in the photocatalytic H_2 production.

3.5 Reaction mechanism for simultaneous BAD and H_2 production over fcc Ru/TiO_2

The reaction mechanism behind the simultaneous photocatalytic BAD and H_2 production over 0.60 wt% fcc Ru/TiO_2 was studied in more detail by performing a series of blank and control experiments using specific radical scavengers. No BAD and H_2 are produced in absence of a catalyst and/or light, confirming that the reaction is driven by a photocatalytic process (Table S5 (ESI†)). Potassium persulfate ($K_2S_2O_8$) was used as an electron scavenger and ammonium oxalate (AO) as a hole scavenger and added into the reaction system,[52] as shown in Fig. 3B and Table S6 (ESI†). In presence of $K_2S_2O_8$, the generation of H_2 is significantly decreased, while the production of BAD remains unaltered. This can be explained by the reduction of $S_2O_8^{2-}$ to SO_4^{2-} by the photoelectrons, thus competing with the H_2 generation.[45] Notably, both BAD and H_2 production are decreased due to the introduction of AO, demonstrating that the protons for the H_2 production originate from the BA oxidation and that the hole-induced BA oxidation is the rate determining step.

In situ electron paramagnetic resonance (EPR) was performed to further unravel the reaction mechanism by demonstrating the presence of reaction intermediates during the oxidation of BA into BAD by using 5,5-dimethyl-1-pyrroline-*N*-oxide (DMPO) as a spin-trapping agent. As shown in Fig. 3C, six characteristic peaks are detected in the presence of light over the 0.60 wt% hcp Ru/TiO_2 and 0.60 wt% fcc Ru/TiO_2 composites, while no free radical signals are measured in dark. The peaks corresponding to nitrogen hyperfine splitting (α_N) and hydrogen hyperfine splitting (α_H) show the generation of carbon-centered radical intermediates (Fig. 3D).[53] Moreover, the EPR signal intensity for 0.60 wt% fcc Ru/TiO_2 is much stronger than that of 0.60 wt% hcp Ru/TiO_2 under simulated solar light illumination (AM 1.5). This observation is caused by the formation of an increased amount of DMPO-Cα radical, showing that an increased amount of reaction intermediates is formed during the catalytic reaction by the fcc Ru/TiO_2 composite. This demonstrates that loading TiO_2 with fcc Ru NPs accelerates the catalytic reaction much stronger as compared to loading TiO_2 with hcp Ru NPs.

Based on the above observations, the reaction mechanism for the simultaneous photocatalytic BAD and H_2 production from benzaldehyde over fcc Ru/TiO_2 is proposed in Scheme S1 (ESI†). First, TiO_2 excited by solar light generates electron–hole pairs. The photogenerated holes in the valence band (VB) of TiO_2 can oxidize the adsorbed benzyl alcohol to generate carbon-centered radical intermediates and protons. Then, the as-formed radicals will be further oxidized by an extra hole to form BAD. In the meantime, the photogenerated electrons in the conduction band (CB) of TiO_2 will transfer to fcc Ru NPs due to the formation of a Schottky barrier to retard the recombination of charge carriers. The separated electrons will react with the released protons, reducing them to form H_2.

4 Conclusions

In this work, we compared the performance of regular hcp and allotropic fcc Ru NPs as cocatalysts for the simultaneous photocatalytic production of BAD and H_2 from benzyl alcohol over TiO_2. The BAD and H_2 production rates over the optimal 0.60 wt% fcc Ru/TiO_2 composite are 1877 and 1860 μmol g^{-1} h^{-1}, respectively, which are 7.6- and 8.2-times increases over the production rate of pristine TiO_2. This is attributed to the formation of a Schottky barrier between Ru and TiO_2 to efficiently transfer the photogenerated charge carriers. Due to the formation of this Schottky barrier, Ru acts as an electron sink. This causes the electrons to be trapped on the surface of Ru, while the holes remain on the surface of TiO_2. The oxidation of BA to BAD will therefore occur on the surface of TiO_2, while the reduction of protons to H_2 occurs on the surface of Ru. Furthermore, the 0.60 wt% fcc Ru/TiO_2 composite exhibits a 1.9-fold activity enhancement compared to the 0.60 wt% hcp Ru/TiO_2 composite, which is ascribed to the fact that fcc Ru NPs are more efficient in facilitating the charge transfer as compared hcp Ru NPs. In addition, the Schottky barrier height, determined *via* the Schottky–Mott rule, between fcc Ru and TiO_2 (1.2 eV) is higher than that in the hcp Ru/TiO_2 composite (0.3 eV), which is beneficial for retarding the backflow of photoelectrons and facilitates the catalytic reactions, resulting in the improved photoactivity for the 0.60 wt% fcc Ru/TiO_2 composite over the 0.60 wt% hcp Ru/TiO_2 composite.

Author contributions

Michaël Gebruers: conceptualization, methodology, lead investigation, writing – original draft, visualization. Chunhua Wang: supporting investigation. Rafikul A. Saha: formal analysis Yangshan Xie: supporting investigation. Imran Aslam: supporting investigation. Li Sun: supporting investigation. Yuhe Liao: supporting investigation. Xuhui Yang: supporting investigation Taoran Chen: supporting investigation. Min-Quan Yang: supervision. Bo Weng: conceptualization, writing – review & editing, supporting investigation. Maarten B. J. Roeffaers: conceptualization, validation, resources, writing – review & editing, supervision, project administration, funding acquisition.

Conflicts of interest

There are no conflicts to declare.

Acknowledgements

This work was financially supported by the Research Foundation – Flanders (FWO grants G098319N, 1280021N), the KU Leuven Research Fund (C14/19/079, iBOF-21-085 PERSIST), and KU Leuven Industrial Research Fund (C3/19/046).

References

1 L. Wang, X. Zhang, L. Yang, C. Wang and H. Wang, *Catal. Sci. Technol.*, 2015, **5**, 4800–4805.
2 S. Higashimoto, N. Kitao, N. Yoshida, T. Sakura, M. Azuma, H. Ohue and Y. Sakata, *J. Catal.*, 2009, **266**, 279–285.
3 A. Fujishima, X. Zhang and D. A. Tryk, *Surf. Sci. Rep.*, 2008, **63**, 515–582.
4 F. Zhang, X. Wang, H. Liu, C. Liu, Y. Wan, Y. Long and Z. Cai, *Appl. Sci.*, 2019, **9**, 2489.
5 C. Wang, B. Weng, M. Keshavarz, M. Q. Yang, H. Huang, Y. Ding, F. Lai, I. Aslam, H. Jin, G. Romolini, B. L. Su, J. A. Steele, J. Hofkens and M. B. J. Roeffaers, *ACS Appl. Mater. Interfaces*, 2022, **14**, 17185–17194.
6 S. Lu, B. Weng, A. Chen, X. Li, H. Huang, X. Sun, W. Feng, Y. Lei, Q. Qian and M. Q. Yang, *ACS Appl. Mater. Interfaces*, 2021, **13**, 13044–13054.
7 S. Zhong, Y. Xi, S. Wu, Q. Liu, L. Zhao and S. Bai, *J. Mater. Chem. A*, 2020, **8**, 14863–14894.
8 S. Wang, Y. Zhang, Y. Zheng, Y. Xu, G. Yang, S. Zhong, Y. Zhao and S. Bai, *Small*, 2022, **2204774**, 1–13.
9 T. Chen, M. Li, L. Shen, M. B. J. Roeffaers, B. Weng, H. Zhu, Z. Chen, D. Yu, X. Pan, M. Q. Yang and Q. Qian, *Front. Chem.*, 2022, **10**, 833784.
10 J. Ran, M. Jaroniec and S. Z. Qiao, *Adv. Mater.*, 2018, **30**, 1704649.
11 J. Yang, D. Wang, H. Han and C. Li, *Acc. Chem. Res.*, 2013, **46**, 1900–1909.
12 L. L. Tan, W. J. Ong, S. P. Chai and A. R. Mohamed, *Appl. Catal., B*, 2015, **166–167**, 251–259.
13 J. Long, H. Huang, J. Zhao, B. Weng, F. Lai, M. Zhang, J. Hofkens, M. B. J. Roeffaers and J. A. Steele, *Angew. Chem., Int. Ed.*, 2022, **61**, e202204563.
14 J. Tian, J. Li, N. Wei, X. Xu, H. Cui and H. Liu, *Ceram. Int.*, 2016, **42**, 1611–1617.
15 M. Ismael, *New J. Chem.*, 2019, **43**, 9596–9605.
16 K. Guo, X. Zhu, L. Peng, Y. Fu, R. Ma, X. Lu, F. Zhang, W. Zhu and M. Fan, *Chem. Eng. J.*, 2021, **405**, 127011.
17 S.-T. Zhang, C.-M. Li, H. Yan, M. Wei, D. G. Evans and X. Duan, *J. Phys. Chem. C*, 2014, **118**, 3514–3522.
18 G. Viau, L. Brayner, L. Poul, N. Chakroune, E. Lacaze, F. Fievet-Vincent and F. Fievet, *Chem. Mater.*, 2003, **15**, 486–494.
19 K. Kusada, H. Kobayashi, T. Yamamoto, S. Matsumura, K. Sato, K. Nagaoka, Y. Kubota and H. Kitagawa, *J. Am. Chem. Soc.*, 2013, **135**, 5493–5496.
20 Z. Fan and H. Zhang, *Acc. Chem. Res.*, 2016, **49**, 2841–2850.
21 Z. Fan and H. Zhang, *Chem. Soc. Rev.*, 2016, **45**, 63–82.
22 M. Zhao and Y. Xia, *Nat. Rev. Mater.*, 2020, **5**, 440–459.
23 H. Li, X. Zhou, W. Zhai, S. Lu, J. Liang, Z. He, H. Long, T. Xiong, H. Sun, Q. He, Z. Fan and H. Zhang, *Adv. Energy Mater.*, 2020, **10**, 2002019–2002030.
24 J. Liu, Q. Ma, Z. Huang, G. Liu and H. Zhang, *Adv. Mater.*, 2019, **31**, 1800696–1900715.
25 F. Ye, F. Wang, C. Meng, L. Bai, J. Li, P. Xing, B. Teng, L. Zhao and S. Bai, *Appl. Catal., B*, 2018, **230**, 145–153.
26 W. Shang, Y. Li, H. Huang, F. Lai, M. B. J. Roeffaers and B. Weng, *ACS Catal.*, 2021, **11**, 4613–4632.
27 J. Hafner, *J. Comput. Chem.*, 2008, **29**, 2044–2078.
28 G. Kresse and J. Hafner, *Phys. Rev. B: Condens. Matter Mater. Phys.*, 1993, **48**, 13115–13118.
29 J. P. Perdew, K. Burke and Y. Wang, *Phys. Rev. B: Condens. Matter Mater. Phys.*, 1996, **54**, 16533–16539.
30 M. Zhao, Z. D. Hood, M. Vara, K. D. Gilroy, M. Chi and Y. Xia, *ACS Nano*, 2019, **13**, 7241–7251.
31 H. Ye, Q. Wang, M. Catalano, N. Lu, J. Vermeylen, M. J. Kim, Y. Liu, Y. Sun and X. Xia, *Nano Lett.*, 2016, **16**, 2812–2817.
32 M. Kumar, P. Devi and V. D. Shivling, *Mater. Res. Express*, 2017, **4**, 085006.
33 W. Z. Li, J. X. Liu, J. Gu, W. Zhou, S. Y. Yao, R. Si, Y. Guo, H. Y. Su, C. H. Yan, W. X. Li, Y. W. Zhang and D. Ma, *J. Am. Chem. Soc.*, 2017, **139**, 2267–2276.
34 Z. Wu and H. Jiang, *RSC Adv.*, 2015, **5**, 34622–34629.
35 U. Balachandran and N. G. Eror, *J. Solid State Chem.*, 1982, **42**, 276–282.
36 S. K. Khore, S. R. Kadam, S. D. Naik, B. B. Kale and R. S. Sonawane, *New J. Chem.*, 2018, **42**, 10958–10968.
37 B. Liu, X. Li, Q. Zhao, J. Ke, M. Tadé and S. Liu, *Appl. Catal., B*, 2016, **185**, 1–10.
38 M. Zhao, Z. Chen, Z. Lyu, Z. D. Hood, M. Xie, M. Vara, M. Chi and Y. Xia, *J. Am. Chem. Soc.*, 2019, **141**, 7028–7036.
39 B. Weng, Q. Quan and Y. J. Xu, *J. Mater. Chem. A*, 2016, **4**, 18366–18377.

40 C. Liu, K. S. Kim, J. Baek, Y. Cho, S. Han, S. W. Kim, N. K. Min, Y. Choi, J. U. Kim and C. J. Lee, *Carbon*, 2009, **47**, 1158–1164.
41 A. T. Kuvarega, R. W. M. Krause and B. B. Mamba, *J. Phys. Chem. C*, 2011, **115**, 22110–22120.
42 W. Qi, C. Wang, J. Yu, S. Adimi, T. Thomas, H. Guo, S. Liu and M. Yang, *ACS Appl. Energy Mater.*, 2022, **5**, 6155–6162.
43 L. Peng, C. Yu, Y. Ma, G. Xie, X. Xie, Z. Wu and N. Zhang, *Inorg. Chem. Front.*, 2022, **9**, 994–1005.
44 S. Liu, W. Qi, S. Adimi, H. Guo, B. Weng, J. P. Attfield and M. Yang, *ACS Appl. Mater. Interfaces*, 2021, **13**, 7238–7247.
45 T. Chen, B. Weng, S. Lu, H. Zhu, Z. Chen, L. Shen, M. B. J. Roeffaers and M. Q. Yang, *J. Phys. Chem. Lett.*, 2022, **13**, 6559–6565.
46 H. Wang, P. Hu, J. Zhou, M. B. J. Roeffaers, B. Weng, Y. Wang and H. Ji, *J. Mater. Chem. A*, 2021, **9**, 19984–19993.
47 S. Liu, W. Kuang, X. Meng, W. Qi, S. Adimi, H. Guo, X. Guo, E. Pervaiz, Y. Zhu, D. Xue and M. Yang, *Chem. Eng. J.*, 2021, **416**, 129116.
48 Y. Huang, Y. Zhu, S. Chen, X. Xie, Z. Wu and N. Zhang, *Adv. Sci.*, 2021, **8**, 2003626.
49 X. Li, L. Chen, J. Wang, J. Zhang, C. Zhao, H. Lin, Y. Wu and Y. He, *J. Colloid Interface Sci.*, 2022, **618**, 362–374.
50 C. Li, W. Chen, M. Li, Q. Sun and Y. Jia, *New J. Phys.*, 2015, **17**, 053006.
51 H. Lin, J. X. Liu, H. Fan and W. X. Li, *J. Phys. Chem. C*, 2020, **124**, 11005–11014.
52 H. Huang, H. Yuan, J. Zhao, G. Solís-Fernández, C. Zhou, J. W. Seo, J. Hendrix, E. Debroye, J. A. Steele, J. Hofkens, J. Long and M. B. J. Roeffaers, *ACS Energy Lett.*, 2019, **4**, 203–208.
53 Q. Guo, F. Liang, X. B. Li, Y. J. Gao, M. Y. Huang, Y. Wang, S. G. Xia, X. Y. Gao, Q. C. Gan, Z. S. Lin, C. H. Tung and L. Z. Wu, *Chem*, 2019, **5**, 2605–2616.